Pharmaceutical Sciences and Drug Design
ISSN: 3062-4428
2024, Volume 4, Page No: 230-248

Available online at: www.galaxypub.co/page/journals

Galaxy Publication

Galaxy Publication

QSAR-Guided Identification of Novel Triazole Derivatives as Potent α-Glucosidase Inhibitors with Favorable ADMET Profiles

Maria Gonzalez[1]*, Javier Ruiz[2], Lucia Torres[1], Daniel Moreno[2]

[1]Department of Pharmaceutical Technology, Faculty of Pharmacy, University of Granada, Granada, Spain.
[2]Department of Medicinal Chemistry, Faculty of Pharmacy, University of Seville, Seville, Spain.

***E-mail** ✉ maria.gonzalez@outlook.com

Received: 21 May 2024; **Revised:** 09 September 2024; **Accepted:** 14 September 2024

ABSTRACT

Due to the rising incidence of diabetes mellitus and the drawbacks of existing therapies, there is an urgent demand for new therapeutic agents targeting this condition. This research concentrates on developing novel compounds with potent alpha-glucosidase inhibitory activity, a key enzyme in managing diabetes. A series of 33 triazole derivatives was subjected to comprehensive QSAR analysis to determine the critical factors affecting their α-glucosidase inhibitory potency. Based on the multiple linear regression (MLR) model, seven potential drug candidates were designed. Molecular docking and dynamics simulations were performed to elucidate the interaction mechanisms between the ligands and the target enzyme, as well as the stability of the resulting complexes. In addition, the pharmacokinetic profiles of these designed compounds were evaluated to forecast their in vivo behavior. Binding free energies were computed using the MMGBSA method, indicating favorable thermodynamic characteristics. The findings identified three new compounds exhibiting high biological activity, strong binding affinity to the target enzyme, and good oral bioavailability. These outcomes provide promising opportunities for developing effective and well-tolerated antidiabetic drugs.

Keywords: Diabetes mellitus, Molecular docking, ADMET, QSAR, Dynamics simulation, Triazoles

How to Cite This Article: Gonzalez M, Ruiz J, Torres L, Moreno D. QSAR-Guided Identification of Novel Triazole Derivatives as Potent α-Glucosidase Inhibitors with Favorable ADMET Profiles. Pharm Sci Drug Des. 2024;4:239-48. https://doi.org/10.51847/jluA9dekev

Introduction

Diabetes mellitus (DM) is a chronic metabolic condition marked by hyperglycemia resulting from impaired insulin action, insufficient insulin production, or a combination of both [1]. Persistent hyperglycemia exacerbates the complications of diabetes mellitus, promoting various macrovascular issues such as peripheral and autonomic neuropathy, heightened risk of atherosclerosis, cerebrovascular disorders, neuropathy, nephropathy, and retinopathy [2].

The primary characteristics of diabetes mellitus (DM) are often accompanied by symptoms like polyuria, polyphagia, weight loss, and blurred vision.

As reported by the IDF Diabetes Atlas (International Diabetes Federation), approximately 436 million individuals globally were living with diabetes in 2021, with projections suggesting this figure could rise to 700 million by 2045 [3, 4].

The development of diabetes mellitus is associated with multiple lifestyle risk factors, including smoking, excessive alcohol intake, sedentary behavior, and comorbidities such as dyslipidemia and hypertension. Genetic factors, stress, and obesity also play significant roles in increasing susceptibility [5], whereas enzymes like alpha-glucosidase and amylase facilitate the breakdown of carbohydrates into glucose and maltose, thereby elevating blood glucose levels, leading to hyperglycemia and interfering with normal insulin function [2].

Simultaneous inhibition of α-glucosidase and α-amylase represents the preferred approach for mitigating the long-term consequences of type 2 diabetes [6]. α-Glucosidase, a major carbohydrate-digesting enzyme located in the intestinal brush border, converts complex oligosaccharides into absorbable monosaccharides [7].

By slowing carbohydrate absorption in the small intestine, alpha-glucosidase inhibitors enable the pancreas to secrete insulin in a more regulated manner. Their antihyperglycemic action is moderate, as they do not stimulate insulin release directly but instead hinder alpha-glucosidase-mediated digestion of complex carbohydrates. Nevertheless, currently available alpha-glucosidase inhibitors, including Miglitol, Acarbose, and Voglibose, are linked to several unwanted side effects, such as nausea, abdominal distension, and flatulence [8, 9].

The diverse biological properties of 1,2,4-triazoles and their fused heterocyclic analogs have drawn considerable interest from both academic and industrial researchers, making them a prominent class among nitrogen-containing heterocycles [10]. Several approved drugs with therapeutic importance contain the 1,2,4-triazole scaffold, including Sitagliptin, Voriconazole, and Fluconazole [11, 12].

A triazole is a five-membered heterocyclic ring comprising three nitrogen atoms and two carbon atoms linked by alternating π-bonds, with the molecular formula C2H3N3. Triazoles exhibit pharmacological features such as moderate dipole moment, hydrogen-bonding capability, ion–dipole interactions, π–π stacking, cation–π interactions, hydrophobic interactions, van der Waals forces, rigidity, and metabolic stability [13].

In 2020, Emmanuel Oloruntoba Yeye *et al*. synthesized various 1,2,4-triazole derivatives and determined their IC50 values through experimental testing [14]. The primary goal of the present study is to identify novel 1,2,4-triazole-based compounds with potent α-glucosidase inhibitory activity. Specifically, a 2D-QSAR analysis was conducted on these derivatives to develop predictive models for designing new triazole compounds and estimating their biological activities prior to synthesis [15, 16].

Materials and Methods

A collection of 33 substituted 1,2,4-triazole derivatives was obtained from an earlier publication [14]. These molecules demonstrated moderate to high inhibitory activity toward α-glucosidase, with their IC_{50} values converted to pIC_{50} ($-\log IC_{50}$) for QSAR development, as detailed in **Table 1.** The chemical structures of these derivatives were constructed and geometry-optimized using the MMFF94 force field in Chem3D version 19.0.0.22 [17].

Table 1. Two-dimensional structures of the 33 triazole derivatives along with their corresponding pIC_{50} values against alpha-glucosidase.

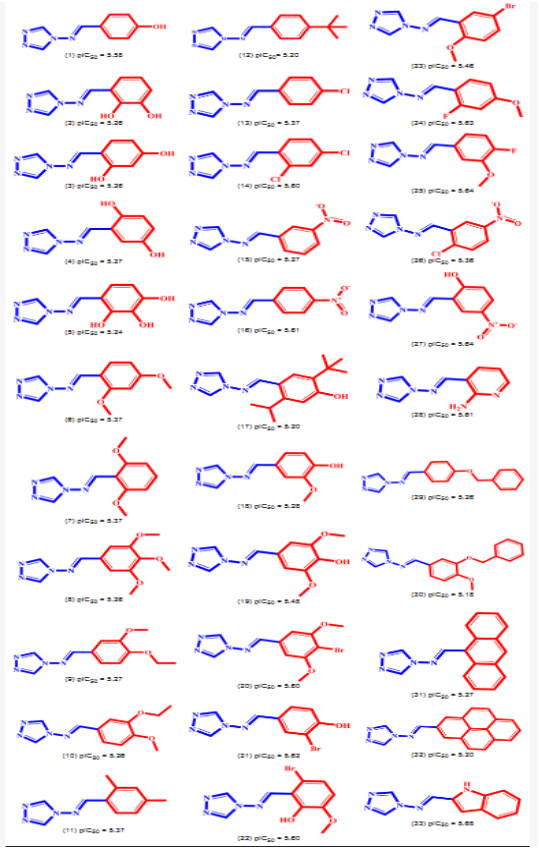

Molecular descriptor computation and pruning

Molecular descriptors were generated for all compounds with the PaDEL software [18]. Since PaDEL computes more than 800 descriptors per molecule, a selection process was necessary to retain only relevant features. The objective feature selection tool in QSARINS software was applied for this purpose [19]. Descriptors showing high pairwise correlation ($|r| > 0.90$) or near-constant values (>95%) were removed to eliminate multicollinearity and irrelevant variables in subsequent GA-MLR modeling. Following pruning, a final set of 433 descriptors covering 1D and 2D categories was kept [20, 21].

QSAR model construction and validation

QSAR models were developed using QSARINS software, which is recognized for generating robust genetic algorithm-multiple linear regression (GA-MLR) models. The dataset was randomly partitioned into training (80%) and test (20%) sets via the software's random split function [22, 23]. This established approach allows model training on one subset and evaluation on an independent group [24].

The strategy focused on incorporating the optimal number of descriptors that significantly influence biological activity to maximize model performance [25]. Descriptors served as independent variables to predict activity according to Eq. 1:

$$Y = a_0 + a_1X_1 + a_2X_2 \quad (1)$$

Models were rigorously validated internally and externally, including Y-randomization and applicability domain assessment, in line with OECD principles [26, 27]. Performance was evaluated using multiple statistical metrics to identify the optimal model, including adjusted R^2 (R^2_adj), external R^2 (R^2_test), root-mean-square error (RMSE), and determination coefficient (R^2). The leave-one-out cross-validation coefficient (Q^2_LOO) was employed as the fitness criterion. Values exceeding 0.6 for these parameters generally indicate reliable and robust models [28-30].

The applicability domain (AD) was defined via leverage analysis presented as a Williams plot, plotting standardized residuals against leverage values. The critical leverage threshold was calculated as $h^* = 3(k + 1)/n$, where n is the number of training compounds and k is the number of descriptors. Compounds within this domain are considered suitable for reliable predictions [31, 32].

Molecular docking

Molecular docking was employed to identify preferred binding poses of the ligands within the target active site, along with binding affinities and specific residue interactions [33].

The protein structure was downloaded from the Protein Data Bank with PDB ID 2f6d [34], representing the glucoamylase from Saccharomycopsis fibuligera complexed with Acarbose. This structure was selected due to its similarity to alpha-glucosidase inhibition by Acarbose, combined with high resolution (1.60 Å, below 2 Å). The receptor consists of 492 residues in Chain A (glucoamylase) **(Figure 1a)**. Heteroatoms including alpha-acarbose, phosphate, and sodium ions were removed prior to docking [34].

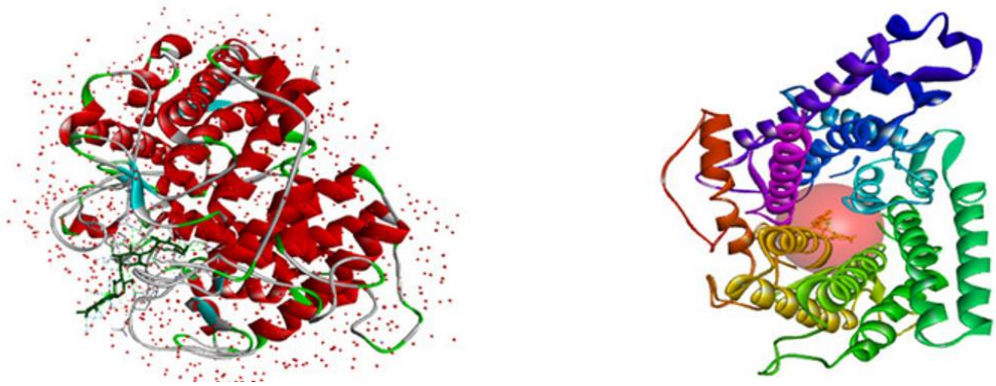

a) b)

Figure 1. (a) Three-dimensional structure of the 2f6d receptor; (b) active site location in the 2f6d receptor.

Protein preparation involved energy minimization with Swiss-PDB Viewer [35], addition of polar hydrogens, and assignment of Gasteiger charges using AutoDock Vina [36-38]. Water molecules present in the binding pocket were retained to allow potential bridging interactions with ligands. Ligands were energy-minimized under the MMFF94 force field using Avogadro software [39] to achieve optimal conformations.

The docking grid was centered on the co-crystallized Acarbose position, a known alpha-glucosidase inhibitor used as reference [40]. Grid coordinates were set at x = 12.68 Å, y = 10.80 Å, z = −6.35 Å, with dimensions of 20 $Å^3$ and spacing of 0.375 Å **(Figure 1b).**

Docking was performed in five independent runs for reproducibility. Final ligand poses were chosen based on cluster frequency across runs. All selected poses appeared consistently in every run, confirming their reliability. **Figure 2** illustrates the occurrence frequency of the resulting conformations across the runs.

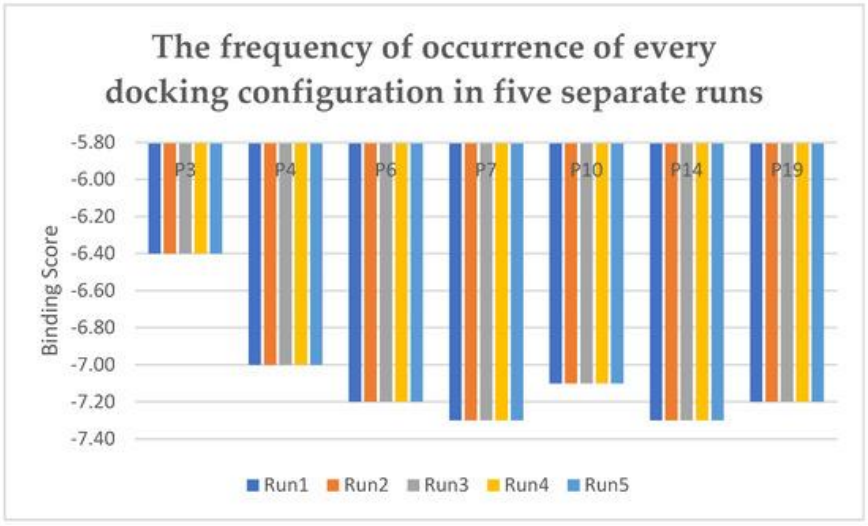

Figure 2. Occurrence frequency of each docking pose across five separate runs.

To validate the docking procedure, the co-crystallized ligand (Acarbose) was first redocked into the receptor's binding pocket [8]. All newly designed compounds were then docked using AutoDock tools [41], allowing detailed examination of possible interactions and calculation of binding affinities within the receptor's active site. Docking was carried out over 9 independent runs, and the pose from the run exhibiting the lowest binding energy—with an RMSD of 0—was chosen for further evaluation [42]. The computed RMSD of 0.217 Å (well below 2 Å) demonstrates close overlap between the original and redocked Acarbose poses **(Figure 3)**. This low deviation confirms the accuracy and reproducibility of the docking methodology in recreating the native binding orientation of the reference inhibitor [43].

Figure 3. Superimposition of the redocked ligand (yellow) onto the co-crystallized ligand (grey), highlighting strong conformational agreement and validating the docking protocol.

ADMET analysis

Compounds displaying high pIC_{50} values against alpha-glucosidase were evaluated for ADMET characteristics to better understand their pharmacokinetic and safety profiles, encompassing absorption, distribution, metabolism,

excretion, and toxicity [44, 45]. Predictions were performed using the widely adopted pkCSM web server, which models compound behavior in vivo.

Compliance with Lipinski's rule of five was checked to filter out unsuitable candidates, requiring molecular weight below 500 g/mol, ≤5 hydrogen bond donors, ≤10 hydrogen bond acceptors, and LogP ≤5 [46]. Additional parameters—including Caco-2 permeability, human intestinal absorption, and steady-state volume of distribution (VDss)—were computed to assess overall drug-likeness and potential performance in the body [46].

Molecular dynamics (MD) simulation

Top-performing compounds—selected based on superior docking scores, highest inhibitory activity, and favorable ADMET profiles—underwent molecular dynamics simulations to monitor structural dynamics via metrics such as Root-Mean-Squared Deviation (RMSD) and Root-Mean-Squared Fluctuation (RMSF). Resulting protein–ligand contacts were analyzed to explain observed stability or conformational changes [47, 48].

Complexes were prepared, energy-minimized, and refined using the OPLS3e force field [49] through the Protein Preparation Wizard in Maestro software [50]. The system was solvated in an orthorhombic box with the TIP3P water model [51]. Na^+ and Cl^- ions were added to neutralize charges, and physiological salt concentration was set to 0.15 M. The system was gradually heated to 300 K at 1 bar pressure employing the Nose–Hoover thermostat and Martyna–Tobias–Klein barostat [52]. Simulations were run for 100 ns under the NPT ensemble with regular trajectory recording, utilizing the Desmond module within Schrödinger 2020-3 academic release [53].

Binding free energies of the simulated complexes were estimated via the Molecular Mechanics/Generalized Born Surface Area (MM/GBSA) method implemented in Maestro. This approach provides valuable thermodynamic insights into ligand–protein binding energetics during dynamics trajectories and enables efficient ranking of interaction strength [54].

Results and Discussion

QSAR model analysis and validation in line with OECD guidelines

Through the application of the GA-MLR technique, multiple predictive models were developed, each incorporating between 4 and 6 descriptors. The most suitable model was identified based on superior statistical metrics that demonstrate its reliability, predictive accuracy, and stability. This optimal model, which utilizes the descriptors AATSC8s, VE3_Dzs, nHsOH, CIC1, and RotBFrac **(Tables 2 and 3)**, fulfilled every validation standard. Key metrics comprised the leave-one-out cross-validation correlation coefficient ($Q^2LOO = 0.633$), the determination coefficient ($R^2 = 0.767$), the root-mean-square error (RMSE = 0.082), the adjusted determination coefficient ($R^2adj = 0.712$), and the determination coefficient for the external test set ($R^2test = 0.649$).

Table 2. The GA-MLR-based model and its associated statistical performance indicators.

Description	Value
QSAR Model Equation	$pIC_{50} = 6.403 + 0.759$ AATSC8s $+ 0.022$ VE3_Dzs $- 0.112$ nHsOH $- 0.338$ CIC1 $- 1.804$ RotBFrac
Total number of compounds	33
Compounds in training set	27
Compounds in test set	6
Model fitting performance	
Coefficient of determination (R^2)	0.767
Adjusted R^2 (R^2_adj)	0.712
Root mean square error (RMSE)	0.082
Internal validation	
Leave-one-out cross-validation (Q^2_LOO)	0.649
External validation	
External R^2 (R^2_ext)	0.633
Randomization test parameters	
Difference $R^2 - R^2$_adj	0.055
Average R (random models)	0.428
Average R^2 (random models)	0.196
Average Q^2 (random models)	−0.342

cRp² (randomization R²)	0.669

Table 3. Interpretation of the molecular descriptors employed in the selected model.

Descriptor Symbol	Name of Descriptor	References
AATSC8s	Average centered Broto-Moreau autocorrelation at lag 8, weighted by I-state	[55]
VE3_Dzs	Logarithmic coefficient sum of the last eigenvector from the Barysz matrix, weighted by I-state	[56]
nHsOH	Number of atom-type H E-State values corresponding to hydroxyl groups (-OH)	[57]
CIC1	Complementary information content (neighborhood symmetry of 1-order)	[58]
RotBFrac	Proportion of rotatable bonds, not including terminal ones	[59]

Outcomes from the Y-randomization procedure confirmed that no randomized model approached the performance of the original one, as evidenced in **Table 2**. The markedly reduced R^2 and Q^2 values in randomized runs, together with their mean values ($R^2YS = 0.195$ and $Q^2YS = -0.341$), verify that the QSAR model does not rely on spurious correlations.

The applicability domain (AD) was defined to outline the chemical space covered by the dataset and to evaluate the reliability of predictions according to structural similarity with the training set molecules. To achieve this, a Williams plot was generated, incorporating a cutoff of three standard deviations and leverage values not exceeding the warning threshold. Accordingly, QSAR predictions are deemed trustworthy solely for compounds situated inside this AD. Assessment indicated that no outliers were present in the response values for either training or test sets. Every compound displayed a leverage below the critical value of $h^* = 0.667$ **(Figure 4)**, with standardized residuals confined within ±3 standard deviations [14].

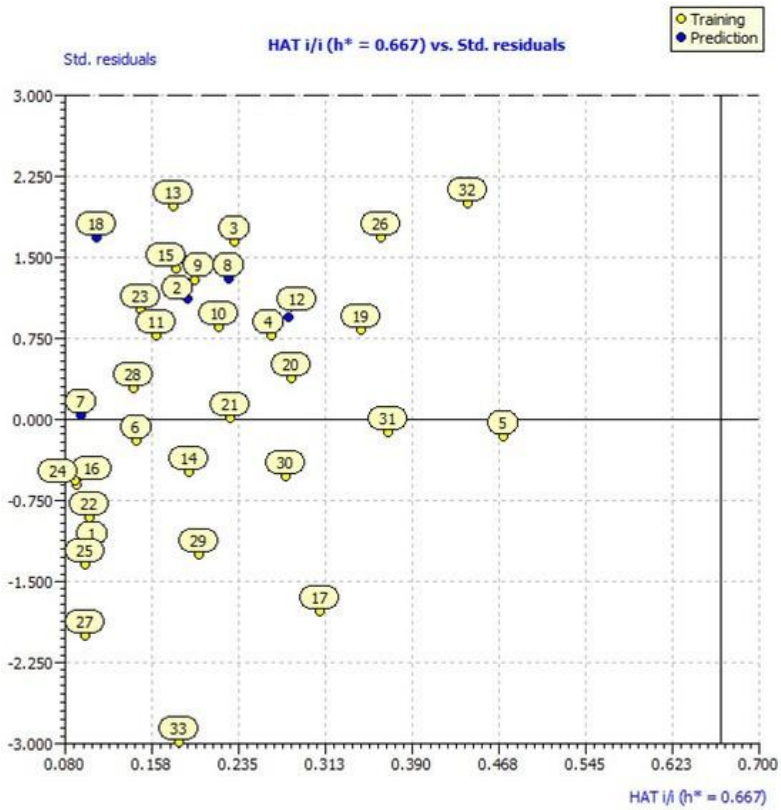

Figure 4. Williams plot for the selected model.

Development of new compounds

An earlier work conducted by Emmanuel Oloruntoba Yeye *et al*. examined the α-glucosidase inhibitory effects of 33 synthesized molecules. Their data revealed that compounds 14, 16, 20, 21, 25, 27, 28, and 33 possessed inhibitory strength on par with the reference agent Acarbose. Common structural features among these potent molecules included halogen atoms, amino functionalities, and/or nitro substituents.

Derivatives containing nitro, amino, or halogen moieties generally exhibited superior inhibition, in contrast to those bearing hydroxy groups, which displayed diminished activity.

Leveraging the validated QSAR model alongside these observations, the present research sought to engineer improved inhibitors of α-glucosidase. The target was to obtain predicted pIC50 values exceeding those of the top-performing compounds from the initial dataset.

Modifications emphasized the introduction of nitro and halogen groups to elevate AATSC8s and VE3_Dzs descriptor values, while deliberately excluding hydroxy substituents owing to their detrimental influence on potency. Concurrently, adjustments were implemented to reduce nHsOH, CIC1, and RotBFrac values. By implementing these guided modifications on the triazole framework, seven promising new structures were proposed, as illustrated in **Table 4**. Relative to the leading compound from the original set **(Table 5),** all newly designed molecules demonstrated superior predicted pIC50 values.

Table 4. Two-dimensional structures of the newly proposed compounds derived from the model.

N	Structure	N	Structure
3	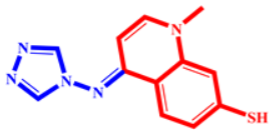	10	
4	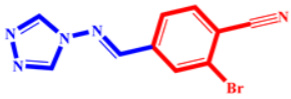	14	
6		19	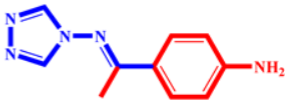
7	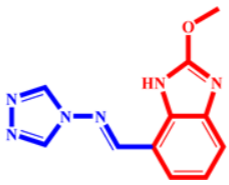		

Table 5. Descriptor values for the model in the original synthesized compounds and the proposed new compounds, including predicted pIC50 and leverage data.

Name	N°	VE3_Dzs	AATSC8s	nHsOH	pIC_{50}	CIC1	RotBFrac	hi
Synthetized Compounds	1 *	−3.819	−0.006	1	5.582	1.439	0.133	h* = 0.667
	2 *	−6.599	−0.010	2	5.264	1.316	0.125	
	3	−7.797	0.037	2	5.264	1.316	0.125	
	4	−8.587	−0.010	2	5.270	1.316	0.125	
	5	−5.287	−0.075	3	5.241	1.328	0.118	
	6	−7.498	0.064	0	5.369	1.578	0.222	
	7 *	−6.004	0.043	0	5.367	1.578	0.222	
	8 *	−4.740	0.184	0	5.263	1.830	0.250	
	9	−5.434	0.131	0	5.271	1.633	0.263	
	10	−7.007	0.122	0	5.262	1.633	0.263	
	11	−3.355	−0.174	0	5.369	1.621	0.125	
	12 *	−1.724	−0.169	0	5.196	1.968	0.167	
	13	−2.264	−0.128	0	5.368	1.507	0.133	
	14	−2.531	−0.128	0	5.604	1.346	0.125	
	15	−7.233	−0.127	0	5.270	1.376	0.177	
	16	−4.375	0.044	0	5.607	1.376	0.177	
	17	−2.618	−0.074	1	5.198	2.214	0.182	
	18 *	−7.781	0.032	1	5.276	1.193	0.176	

	19	−4.965	0.256	1	5.485	1.396	0.211	
	20	−5.270	0.220	0	5.599	1.349	0.211	
	21	−2.950	−0.004	1	5.625	1.103	0.125	
	22	−6.069	−0.021	1	5.599	0.937	0.167	
	23	−3.622	−0.103	0	5.461	1.161	0.176	
	24	−5.284	0.012	0	5.633	1.161	0.176	
	25	−6.839	−0.010	0	5.644	1.161	0.176	
	26	−9.690	−0.127	0	5.359	1.055	0.167	
	27	−6.929	−0.030	1	5.636	1.011	0.167	
	28	−4.901	−0.080	0	5.613	1.069	0.133	
	29	−3.755	0.001	0	5.264	2.216	0.217	
	30	−3.692	−0.037	0	5.184	2.094	0.240	
	31	−4.566	0.000	0	5.267	2.641	0.083	
	32	−4.196	0.026	0	5.201	2.720	0.074	
	33	−7.010	−0.019	0	5.680	1.664	0.111	
Designed compounds	P3	−3.082	−0.106	0	5.780	1.143	0.050	0.084
	P4	−3.524	−0.005	0	5.738	1.103	0.118	0.023
	P6	−3.328	−0.084	0	5.741	0.891	0.125	0.059
	P7	−4.032	0.083	0	5.758	1.036	0.150	0.055
	P10	−5.263	0.077	0	5.852	0.800	0.125	0.082
	P14	−8.222	0.113	0	5.717	1.224	0.100	0.358
	P19	−3.410	0.109	0	5.741	1.318	0.125	0.081

*: test compounds, P: proposed compounds.

Applicability domain

Leverage values were determined for the synthesized compounds using the formula $hi = xi^T \times (X^T \times X)^{-1} \times xi$ (where i = 1, 2, 3... n) and then compared to the critical leverage threshold (h*). A molecule was deemed to reside within the model's applicability domain provided its hi was below h*. The superscript ^{T} signifies matrix or vector transposition for the test compounds, n represents the count of training compounds, and k stands for the number of descriptors employed in the model. Here, xi corresponds to the descriptor matrix of a given test molecule, whereas X is the descriptor matrix compiled from the n training compounds [14]. By applying h* as the cutoff, leverage was assessed for each candidate structure. As shown in **Table 5**, the computed hi values spanned 0.055–0.358, confirming that every compound falls inside the reliable applicability domain.

Molecular docking

All tested compounds underwent docking simulations targeting the active pocket of the receptor protein. Outcomes, presented in **Figures 5 and 6**, **and Table 6**, showed strong binding energies across the formed complexes, driven by multiple types of contacts between the docked molecules and essential amino acids in the pocket. To serve as a benchmark, Acarbose—a established inhibitor of alpha-glucosidase—was also docked. Its complex with 2f6d displayed key contacts: five Conventional Hydrogen Bonds involving Arg69, Glu211, Glu210, Leu208, and Asp70; two Carbon–Hydrogen Bonds with Trp209 and Ala138; and one Pi–Sigma contact with Tyr351. These contacts occurred at distances of 1.84 Å to 3.79 Å. Furthermore, several Water Hydrogen Bonds were present, emphasizing the contribution of solvent molecules to complex stability.

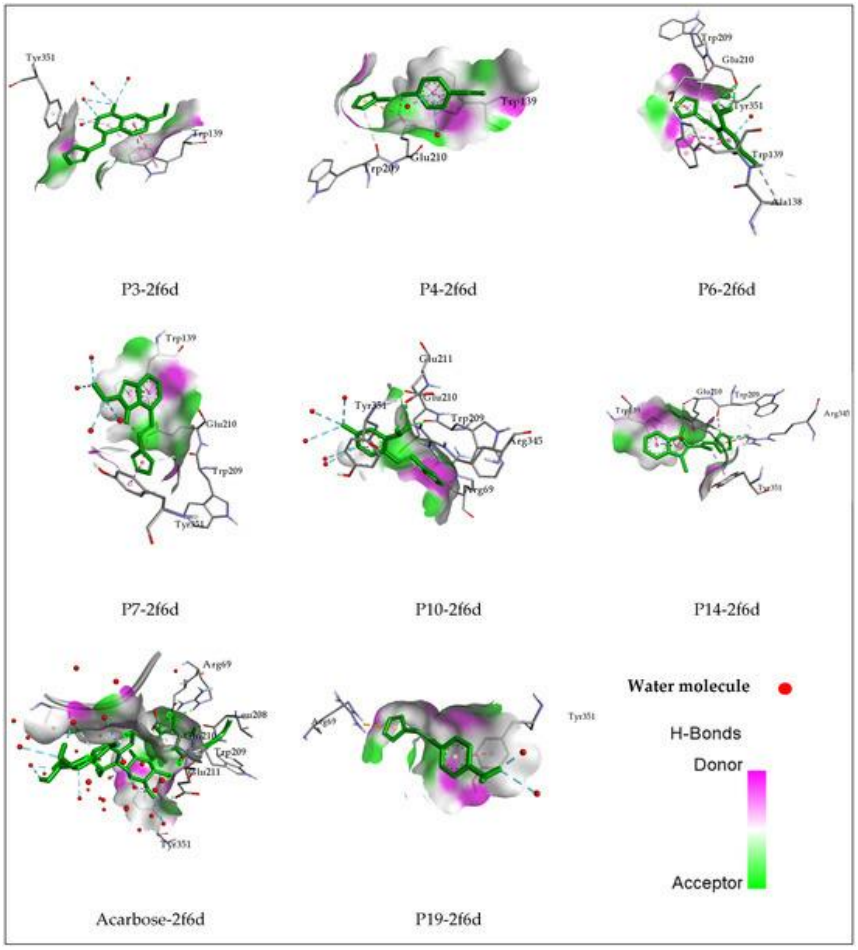

Figure 5. 3D view illustrating ligand positioning inside the alpha-glucosidase binding pocket.

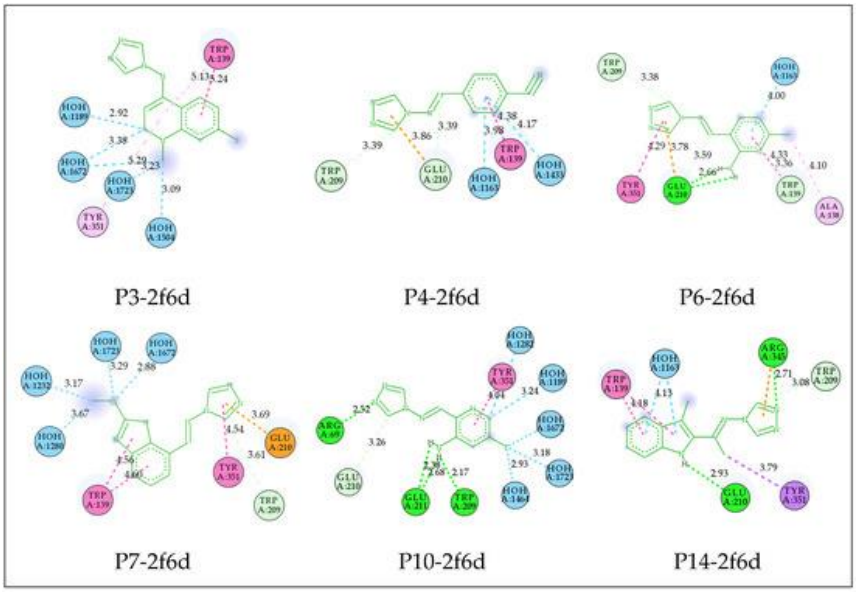

a)

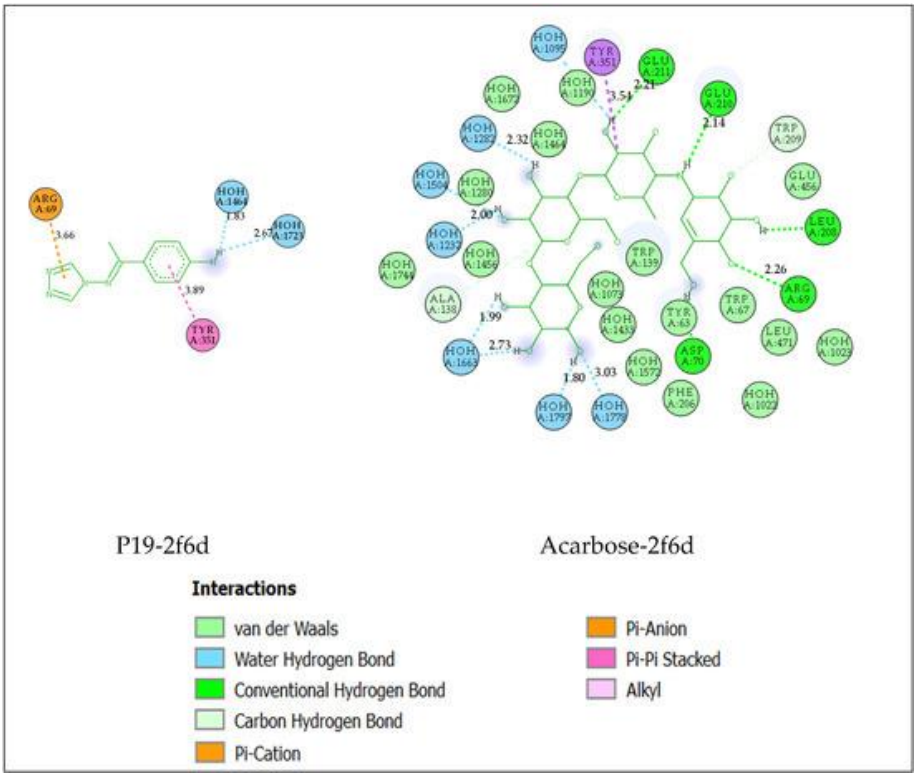

b)

Figure 6. 2D diagrams of the docked complexes, highlighting interaction distances, types, and involved amino acids.

Table 6. Detailed listing of binding energies, interacting residues, interaction categories, and distances (in Å) for the generated complexes.

N	Score Kcal/Mol	Interaction Type	Residue	Distance (Å)
P3	−6.4	Pi–Pi Stacked	Trp139	4.87
		Pi–Pi Stacked	Trp139	4.19
		Pi–Alkyl	Trp139	5.13
		Pi–Alkyl	Tyr351	5.29
		Water Hydrogen Bond	HOH1163	3.57
		Water Hydrogen Bond	HOH1189	2.92
		Water Hydrogen Bond	HOH1672	3.38
		Water Hydrogen Bond	HOH1504	3.09
		Water Hydrogen Bond	HOH1672	3.45
		Water Hydrogen Bond	HOH1723	3.23
P4	−7	Carbon–Hydrogen Bond	Trp209	3.39
		Carbon–Hydrogen Bond	Glu210	3.39
		Pi–Anion	Glu210	3.85
		Pi–Pi Stacked	Trp139	3.85
		Pi–Pi Stacked	Trp139	4.36
		Water Hydrogen Bond	HOH1433	4.17
P6	−7.2	Conventional Hydrogen Bond	Glu210	2.62
		Conventional Hydrogen Bond	Glu210	2.66
		Carbon–Hydrogen Bond	Trp139	3.36
		Carbon–Hydrogen Bond	Trp209	3.38
		Carbon–Hydrogen Bond	Glu210	3.59
		Pi–Anion	Glu210	3.77
		Pi–Pi Stacked	Trp139	4.59
		Pi–Pi Stacked	Trp139	3.97
		Pi–Pi Stacked	Tyr351	4.29
		Alkyl	Ala138	4.1

		Water Hydrogen Bond	HOH1163	4
P7	−7.3	Carbon–Hydrogen Bond	Trp209	3.61
		Pi–Anion	Glu210	3.69
		Pi–Pi Stacked	Trp139	4.43
		Pi–Pi Stacked	Trp139	3.74
		Pi–Pi Stacked	Tyr351	4.54
		Pi–Pi Stacked	Trp139	4.56
		Water Hydrogen Bond	HOH1282	3.81
		Water Hydrogen Bond	HOH1672	2.88
		Water Hydrogen Bond	HOH1723	3.29
		Water Hydrogen Bond	HOH1232	3.17
		Water Hydrogen Bond	HOH1280	3.67
P10	−7.1	Conventional Hydrogen Bond	Arg69	2.52
		Conventional Hydrogen Bond	Trp209	2.17
		Conventional Hydrogen Bond	Glu211	2.68
		Conventional Hydrogen Bond	Glu211	2.38
		Carbon–Hydrogen Bond	Glu210	3.26
		Pi–Pi Stacked	Tyr351	4.04
		Water Hydrogen Bond	HOH1464	2.93
		Water Hydrogen Bond	HOH1672	3.48
		Water Hydrogen Bond	HOH1723	3.18
		Water Hydrogen Bond	HOH1189	3.24
		Water Hydrogen Bond	HOH1282	3.39
P14	−7.3	Conventional Hydrogen Bond	Arg345	2.71
		Conventional Hydrogen Bond	Glu210	2.93
		Carbon–Hydrogen Bond	Trp209	3.08
		Pi–Cation	Arg345	3.42
		Pi–Sigma	Tyr351	3.79
		Pi–Pi Stacked	Trp139	5.27
		Pi–Pi Stacked	Trp139	4.73
		Pi–Pi Stacked	Trp139	3.97
		Pi–Pi Stacked	Trp139	4.45
P19	−7.2	Pi–Cation	Arg69	3.66
		Pi–Pi Stacked	Tyr351	3.89
		Water Hydrogen Bond	HOH1723	2.67
		Water Hydrogen Bond	HOH1464	1.83
Acarbose	−12.3	Conventional Hydrogen Bond	Arg69	2.25
		Conventional Hydrogen Bond	Glu211	2.21
		Conventional Hydrogen Bond	Glu210	2.14
		Conventional Hydrogen Bond	Leu208	1.9
		Conventional Hydrogen Bond	Asp70	1.84
		Carbon–Hydrogen Bond	Trp209	3.52
		Carbon–Hydrogen Bond	Ala138	3.79
		Pi–Sigma	Tyr351	3.54
		Water Hydrogen Bond	HOH1449	2.72
		Water Hydrogen Bond	HOH1504	2.91
		Water Hydrogen Bond	HOH1778	3.03
		Water Hydrogen Bond	HOH1797	1.8
		Water Hydrogen Bond	HOH1663	2.73
		Water Hydrogen Bond	HOH1663	1.99
		Water Hydrogen Bond	HOH1232	2
		Water Hydrogen Bond	HOH1282	2.32
		Water Hydrogen Bond	HOH1095	3.01

The variety of contacts detected—such as Conventional Hydrogen Bonds, Carbon–Hydrogen Bonds, Pi–Sigma linkages with critical residues, plus bridging Water Hydrogen Bonds—points to a highly elaborate binding

interface in the enzyme's active region. These contacts appear vital for disrupting alpha-glucosidase function. The robust affinities and selective binding patterns observed suggest that the compounds could inhibit the enzyme effectively, supporting their possible use in managing alpha-glucosidase-related conditions.

Within the binding pocket, Compound P3 formed several hydrophobic contacts, specifically two Pi–Pi Stacked and two Pi–Alkyl interactions with Trp139 and Tyr351. It also showed Water Hydrogen Bonds to HOH1163, HOH1189, HOH1672, HOH1504, HOH1672, and HOH1723 (distances 2.92–5.29 Å). Compound P4 established contacts including one Carbon–Hydrogen Bond, one Pi–Anion, and Pi–Pi Stacked interactions with Trp209, Glu210, and Trp139, supplemented by a Water Hydrogen Bond to HOH1433. The binding mode of Compound P6 encompassed a broad set of contacts: one Conventional Hydrogen Bond, one Carbon–Hydrogen Bond, Pi–Anion, Pi–Pi Stacked, and Alkyl interactions involving Trp139, Trp209, Glu210, Tyr351, and Ala138, along with a Water Hydrogen Bond to HOH1163. Compound P7's interactions consisted of a Carbon–Hydrogen Bond, Pi–Anion, and Pi–Pi Stacked contacts with Trp209, Glu210, Tyr351, and Trp139, plus Water Hydrogen Bonds to HOH1282, HOH1672, HOH1723, HOH1232, and HOH1280. Compound P10 displayed a Conventional Hydrogen Bond, Carbon–Hydrogen Bond, and Pi–Pi Stacked contacts with Arg69, Trp209, Glu211, Glu210, and Tyr351, together with Water Hydrogen Bonds involving HOH1464, HOH1672, HOH1723, HOH1189, and HOH1282. Compound P14 featured an extensive interaction profile, including one Conventional Hydrogen Bond, one Carbon–Hydrogen Bond, Pi–Cation, Pi–Sigma, and Pi–Pi Stacked contacts with Arg345, Glu210, Trp209, Tyr351, and Trp139. In comparison, Compound 19 primarily relied on Pi–Cation and Pi–Pi Stacked interactions with Arg69 and Tyr351, augmented by Water Hydrogen Bonds to HOH1723 and HOH1464.

Notably, among the evaluated structures, P6, P10, and P14 were found to mimic Acarbose's binding pattern, forming Conventional Hydrogen Bonds, Carbon–Hydrogen Bonds, and Pi–Sigma interactions with identical residues (Arg69, Trp209, Glu210, Glu211, and Tyr351). This overlap in contact profiles indicates that these compounds likely share a similar mode of action with the reference inhibitor, raising the possibility of comparable inhibitory potency against the target enzyme.

ADMET properties prediction

The ADMET profiles of the evaluated compounds were forecasted employing the pkCSM web server. Detailed outcomes are compiled in **Table 7.** Every compound under investigation complied with Lipinski's rule of five.

Table 7. Computed ADMET parameters for the studied compounds via pkCSM online server.

Property	P19	P14	P10	P7	P6	P4	P3
Molecular Weight	201.233	259.7	206.184	242.242	222.639	276.097	257.322
Lipophilicity (LogP)	1.1326	2.6851	0.2766	1.0452	0.7909	1.79448	1.4225
Number of Rotatable Bonds	2	2	2	3	2	2	1
Hydrogen Bond Acceptors	5	4	6	6	6	5	6
Hydrogen Bond Donors	1	1	1	1	1	0	1
Polar Surface Area	87.251	108.105	84.271	102.135	90.409	100.171	108.812
Predicted Water Solubility (log mol/L)	−1.893	−3.667	−2.446	−2.956	−2.684	−3.119	−3.072
Caco-2 Cell Permeability (log Papp)	0.728	1.336	0.74	1.322	1.294	1.011	1.292
Human Intestinal Absorption (% absorbed)	72.544	93.42	85.844	77.072	84.358	97.517	98.134
Skin Permeability (log Kp)	−2.897	−2.72	−2.769	−2.735	−2.84	−2.554	−2.618
P-glycoprotein Substrate	No	Yes	No	Yes	No	No	No
P-glycoprotein I Inhibitor	No	No	No	No	No	No	No
P-glycoprotein II Inhibitor	No	No	No	No	No	No	No
Volume of Distribution (human, log L/kg)	−0.367	−0.195	−0.767	0.051	−0.714	−0.351	−0.294
Plasma Protein Unbound Fraction (human)	0.311	0.215	0.448	0.378	0.448	0.293	0.339
Blood-Brain Barrier Permeability (log BB)	−0.323	0.373	−0.796	−0.587	−0.764	0.149	−0.043
Central Nervous System Permeability (log PS)	−2.414	−2.06	−3.118	−3.456	−3.047	−2.814	−1.977
CYP2D6 Substrate	No	No	No	No	No	No	No
CYP3A4 Substrate	No	Yes	No	No	No	No	Yes
CYP1A2 Inhibitor	Yes	Yes	Yes	Yes	Yes	Yes	Yes
CYP2C19 Inhibitor	No	No	No	No	No	No	No
CYP2C9 Inhibitor	No	No	No	No	No	No	No

CYP2D6 Inhibitor	No	No	No	No	No	No	No
CYP3A4 Inhibitor	No	No	No	No	No	No	No
Total Clearance (log mL/min/kg)	0.239	0.503	0.557	0.586	0.16	0.063	0.109
Renal OCT2 Substrate	No	No	No	Yes	No	No	No
AMES Mutagenicity	Yes	No	No	Yes	No	Yes	Yes
Maximum Recommended Tolerated Dose (human, log mg/kg/day)	0.378	−0.25	0.613	0.593	0.632	0.397	−0.749
hERG I Blocker	No	No	No	No	No	No	No
hERG II Blocker	No	No	No	No	No	No	No
Oral Rat Acute Toxicity (LD50, mol/kg)	2.383	2.51	2.22	1.804	2.379	2.313	2.254
Oral Rat Chronic Toxicity (LOAEL, log mg/kg_bw/day)	1.82	1.669	0.664	1.128	1.604	1.747	1.705
Hepatotoxicity	No	Yes	Yes	Yes	No	No	Yes
Skin Sensitization	No	No	No	No	No	No	No
Tetrahymena pyriformis Toxicity (pIGC50)	0.647	1.002	0.241	0.285	0.284	1.176	0.564
Fathead Minnow Toxicity (LC50, log mM)	2.364	1.28	3.021	2.529	2.684	1.524	2.586

As indicated in **Table 7**, all molecules demonstrated high intestinal absorption, reflecting strong potential for oral bioavailability. Moreover, they exhibited favorable aqueous solubility, which supports efficient uptake. With the exception of Compounds P10 and P19, all displayed robust Caco-2 permeability.

No compound was forecasted to inhibit P-glycoprotein, suggesting minimal interference with efflux pumps responsible for expelling drugs from cells. However, Compounds P7 and P14 were identified as P-glycoprotein substrates, implying they could be recognized and effluxed by this transporter. All molecules showed elevated skin permeation potential, defined by LogKp values exceeding −2.5.

Most compounds had low steady-state volume of distribution (VDss), except for Compounds P3 and P7. Here, low VDss corresponds to LogVDss below −0.15, meaning limited tissue distribution at equilibrium. Only Compound P14 was predicted to readily cross the blood–brain barrier (LogBB > 0.3), while the others showed moderate CNS penetration potential. Compound 3 was deemed capable of entering the central nervous system, whereas Compounds P6, P7, and P10 were classified as non-CNS-penetrant.

Regarding metabolism, all compounds were projected as CYP1A2 inhibitors but neither substrates nor inhibitors of CYP2D6, CYP2C19, CYP2C9, or CYP3A4. Nevertheless, Compounds P6 and P14 emerged as CYP3A4 substrates, indicating possible metabolism by this isoform.

Apart from Compound P7, which was flagged as an OCT2 substrate and thus potentially transported by renal organic cation transporter 2, the remaining compounds were non-substrates for renal OCT2 clearance. Total clearance rates (expressed as Log(ml/min/kg)) varied from 0.063 to 0.586, providing insight into dosing requirements for maintaining steady-state levels.

None of the molecules were anticipated to block hERG I or hERG II channels, reducing the risk of cardiotoxicity via QT prolongation. Additionally, no skin sensitization was predicted, implying low likelihood of contact dermatitis.

In the AMES mutagenicity assay, Compounds P6, P10, and P14 were assessed as non-mutagenic, suggesting negligible risk of inducing bacterial mutations.

Molecular dynamics simulation

Compounds P6, P10, and P14 were chosen for molecular dynamics studies due to their promising ADMET profiles, superior docking scores, and key interactions with critical enzyme residues.

Root-mean-squared deviation

A 100 ns trajectory was generated for the protein–ligand complexes (alpha-glucosidase 2f6d bound to P6, P10, and P14) as well as the apo protein to monitor ligand-induced structural fluctuations. Protein backbone RMSD values were calculated and are displayed in **Figure 7**. Throughout the simulation, RMSD remained steadily below 3 Å, demonstrating equilibrium and conformational stability in the bound states. The consistently low and stable RMSD profile confirms that the ligand-bound complexes preserved structural stability without significant deviations over the entire 100 ns period.

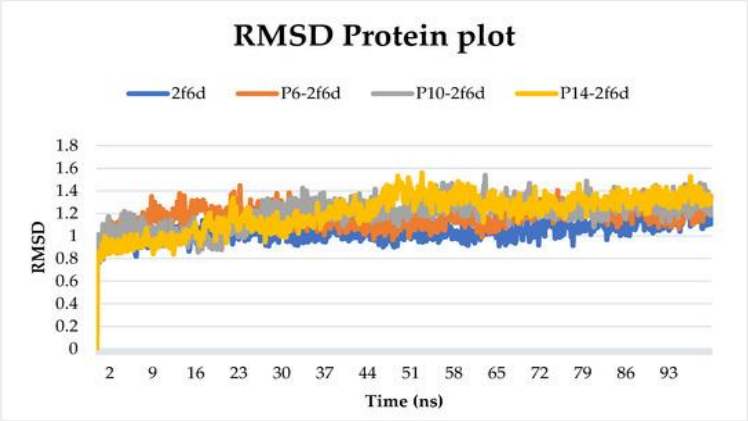

Figure 7. Protein RMSD trajectories for all simulated systems over 100 ns.

Figure 8 displays the RMSD profiles of the bound ligands throughout their association with the receptor. The data indicate sustained stability for P6 and P14, with mean RMSD values of 5.52 Å and 2.82 Å, respectively. Conversely, P10 showed steady behavior during the initial 30 ns, followed by substantial fluctuations surpassing 15 Å, although RMSD eventually declined toward the simulation's conclusion. The overall average RMSD for P10 was 8.16 Å.

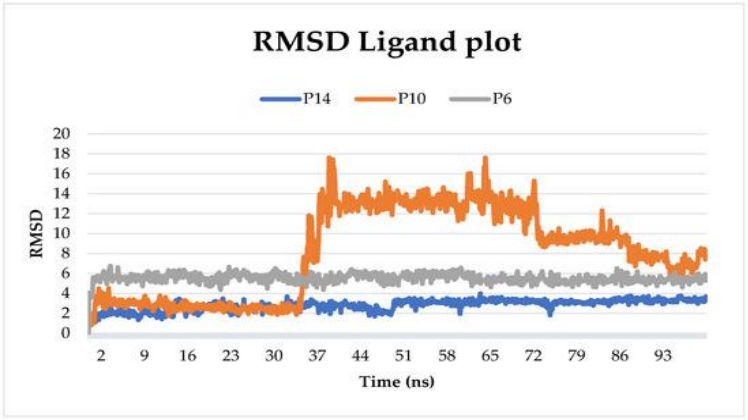

Figure 8. Ligand RMSD trajectories for all simulated systems over 100 ns.

Root-mean-squared fluctuation

Root-Mean-Squared Fluctuation (RMSF) was assessed for each residue across all ligand-bound complexes, with an additional run on the apo protein to enable direct comparison of per-residue mobility. The aim was to determine how the ligands influenced local protein flexibility. Across all complexes, residue RMSF values stayed under 3 Å **(Figure 9)**, reflecting minimal conformational variability. This pattern confirms that protein residues retained high stability in the presence of the bound ligands.

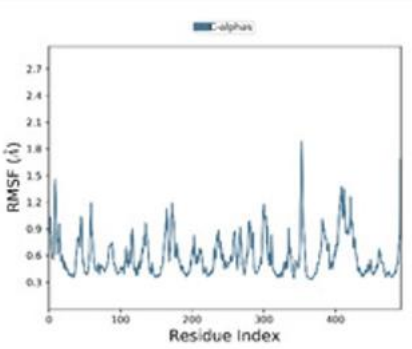

Protein only

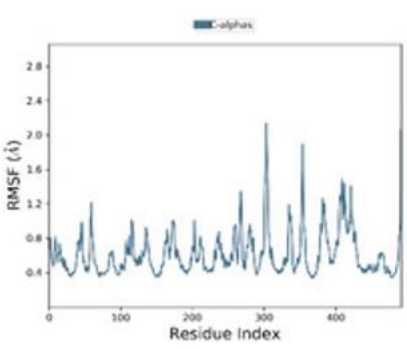

RMSF Protein (P6- Protein)

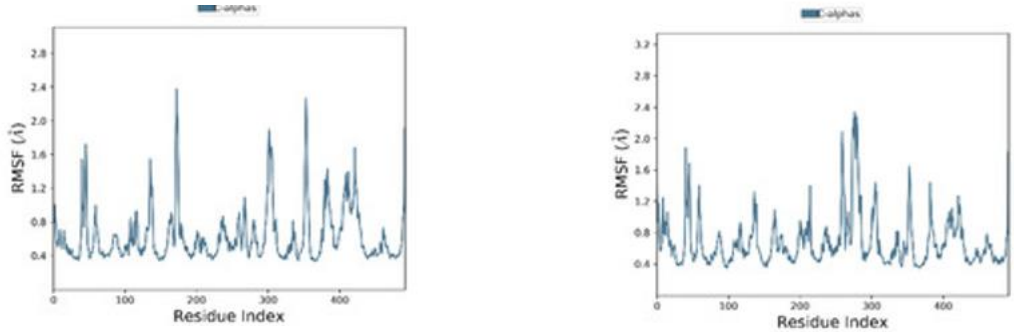

RMSF Protein (P10- 2f6d) RMSF Protein (P6- 2f6d)

Figure 9. Protein RMSF profiles for all simulated systems over 100 ns.

Protein–ligand contact

Detailed mapping of protein–ligand contacts revealed a broad spectrum of interaction types that underpin binding strength, as summarized in **Table 8**. For P6, direct Hydrogen bonds were formed with Tyr63. Hydrophobic contacts dominated with residues Trp209, Tyr351, Trp362, and Trp473, bolstering complex integrity. Ionic interactions occurred with Trp67, Asp70, and Glu210, adding electrostatic contributions. Water-mediated bridges connected the ligand to Tyr63, Arg69, Asp70, Trp209, and Glu210. Notably, contacts with Asp63, Asp70, Trp209, Glu210, Tyr351, and Trp362 persisted throughout the trajectory, emphasizing their importance for sustained complex stability.

Table 8. Histograms and timelines of protein–ligand contacts in all simulated systems over 100 ns (Pink: ionic bond; blue: water bridge; violet: hydrophobic bond; green: Hydrogen bond).

Complex	PL-Contacts Histogram	PL-Contacts Timeline
P6-2f6d	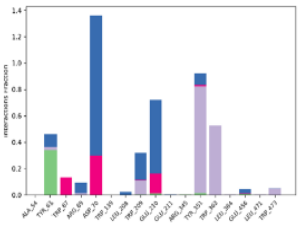	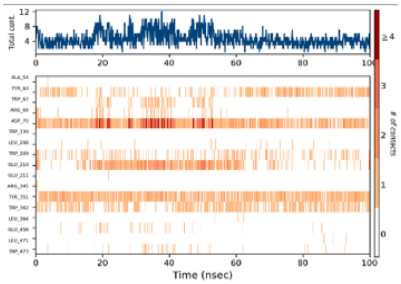
P10-2f6d	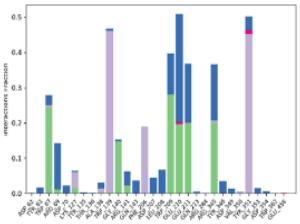	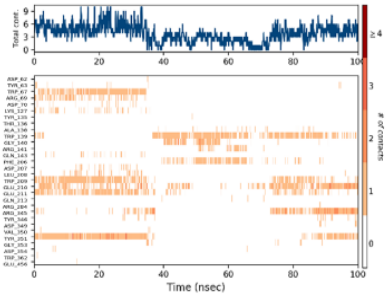
P14-2f6d	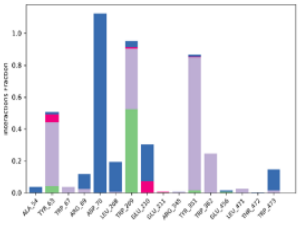	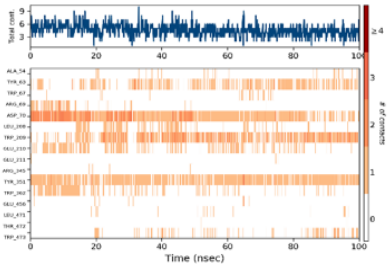

In the P10-2f6d and P14-2f6d systems, multifaceted interaction networks were observed. P10 established Hydrogen bonds with Trp67, Gly140, Trp209, Glu210, Glu211, and Arg345. Water bridges facilitated contacts

involving Arg69, Asp207, Leu208, Trp209, Glu210, Glu211, and Arg345. Hydrophobic interactions with Lys127, Trp139, Phe206, and Tyr351 reinforced stability, while ionic bonds with Glu210 and Tyr351 provided electrostatic support. For P14, ionic contacts were noted with Tyr63 and Glu210. Hydrophobic interactions engaged Tyr63, Trp209, Tyr351, and Trp62. Water bridges linked the ligand to Ala54, Arg69, Asp70, Leu208, Glu210, and Trp473. Direct Hydrogen bonds with Tyr63 and Trp209 further diversified the binding mode. Throughout the simulation, enduring contacts were maintained between P14 and residues Tyr63, Asp70, Trp209, Glu210, and Tyr351, underscoring their critical contribution to the durability of the P14-2f6d complex.

Binding free energy

Calculation of binding free energies for the three complexes—P6-2f6d, P10-2f6d, and P14-2f6d—yielded negative ΔG values of −32.59 kcal/mol, −35.8 kcal/mol, and −41.17 kcal/mol, respectively. These results confirm thermodynamically favorable and spontaneous binding processes. The strongly negative energies reflect robust affinities, with P14-2f6d displaying the most exothermic ΔG, suggesting it forms the most stable and energetically preferred interaction with the receptor protein.

Conclusion

The present work conducted an extensive QSAR study on 33 triazole derivatives to elucidate structural features governing their alpha-glucosidase inhibition. The goal was to discover new candidates for diabetes mellitus treatment. Using the optimal multiple linear regression model, seven novel compounds were proposed and further evaluated through molecular docking and dynamics simulations to probe their binding modes and complex stability with the target enzyme. Pharmacokinetic profiling was performed to forecast absorption, distribution, metabolism, and excretion characteristics. Findings identified three standout compounds (P6, P10, and P14) exhibiting potent inhibitory activity, robust binding to the enzyme, advantageous thermodynamic profiles, and promising oral drug-like properties.

Acknowledgments: None

Conflict of Interest: None

Financial Support: None

Ethics Statement: None

References

1. Sarwar, N.; Gao, P.; Seshasai, S.R.; Gobin, R.; Kaptoge, S.; Di Angelan-tonio, E.; Ingelsson, E.; Lawlor, D.A.; Selvin, E.; Stampfer, M. Emerging risk factors collaboration diabetes mellitus, fasting blood glucose concentration, and risk of vascular disease: A collaborative meta-analysis of 102 prospective studies. *Lancet* **2010**, *375*, 2215–2222.
2. Abchir, O.; Daoui, O.; Nour, H.; Yamari, I.; Elkhattabi, S.; Errougui, A.; Chtita, S. Exploration of cannabis constituents as potential candidates against diabetes mellitus disease using molecular docking, dynamics simulations and Admet investigations. *Sci. Afr.* **2023**, *21*, e014745.
3. International Diabetes Federation. Diabetes Federation. Diabetes around the world in 2021. In *IDF Diabetes Atlas*; International Diabetes Federation: Brussels, Belgium, 2021.
4. Fatima, I.; Taha, M.; Wadood, A.; Mohammad, J.I.; Khan, H. 2-Aryl benzimidazoles: Synthesis, in vitro α-amylase inhibitory activity, and molecular docking study. *Eur. J. Med. Chem.* **2018**, *150*, 248–260.
5. Tanaka, M.; Akiyama, Y.; Mori, K.; Hosaka, I.; Kato, K.; Endo, K.; Ogawa, T.; Sato, T.; Suzuki, T.; Yano, T.; et al. Predictive modeling for the development of diabetes mellitus using key factors in various machine learning approaches. *Diabetes Epidemiology Manag.* **2024**, *13*, 100191.
6. Shadakshari, A.; Kumara, T.S.; Kumar, N.; Chandra, S.J.; Kumar, K.A.; Ramu, R. Synthesis, characterization, and biocomputational assessment of the novel 3-hydroxy-4-(phenyl(pyridin-2-ylamino) methyl)-2-naphthoic acid derivatives as potential dual inhibitors of α-glucosidase and α-amylase enzymes. *Results Chem.* **2023**, *5*, 100745.

7. Gong, L.; Feng, D.; Wang, T.; Ren, Y.; Liu, Y.; Wang, J. Inhibitors of α-amylase and α-glucosidase: Potential linkage for whole cereal foods on prevention of hyperglycemia. *Food Sci. Nutr.* **2020**, *8*, 6320–6337.
8. Abchir, O.; Nour, H.; Daoui, O.; Yamari, I.; ElKhattabi, S.; El Kouali, M.; Talbi, M.; Errougui, A.; Chtita, S. Structure-based virtual screening, ADMET analysis, and molecular dynamics simulation of Moroccan natural compounds as candidates for the SARS-CoV-2 inhibitors. *Nat. Prod. Res.* **2023**, *2023*, 1–8
9. Lee, S.-R.; Choi, J.; Choi, E.-K.; Lee, H.; Han, M.; Ahn, H.-J.; Kwon, S.; Lee, S.-W.; Han, K.-D.; Oh, S.; et al. Early rhythm control on diabetes-related complications and mortality in patients with type 2 diabetes mellitus and atrial fibrillation. *Diabetes Res. Clin. Pract.* **2023**, *206*, 1110200.
10. Chaidam, S.; Saehlim, N.; Athipornchai, A.; Sirion, U.; Saeeng, R. Synthesis and biological evaluation of 1,6-bis-triazole-2,3,4-tri-O-benzyl-α-d-glucopyranosides as a novel α-glucosidase inhibitor in the treatment of Type 2 diabetes. *Bioorganic Med. Chem. Lett.* **2021**, *50*, 128331.
11. Dahmani, R.; Manachou, M.; Belaidi, S.; Chtita, S.; Boughdiri, S. Structural characterization and QSAR modeling of 1,2,4-triazole derivatives as α-glucosidase inhibitors. *N. J. Chem.* **2021**, *45*, 1253–1261.
12. Fallah, Z.; Tajbakhsh, M.; Alikhani, M.; Larijani, B.; Faramarzi, M.A.; Hamedifar, H.; Mohammadi-Khanaposhtani, M.; Mahdavi, M. A review on synthesis, mechanism of action, and structure-activity relationships of 1,2,3-triazole-based α-glucosidase inhibitors as promising anti-diabetic agents. *J. Mol. Struct.* **2022**, *1255*, 132469.
13. Matin, M.M.; Matin, P.; Rahman, R.; Ben Hadda, T.; Almalki, F.A.; Mahmud, S.; Ghoneim, M.M.; Alruwaily, M.; Alshehri, S. Triazoles and Their Derivatives: Chemistry, Synthesis, and Therapeutic Applications. *Front. Mol. Biosci.* **2022**, *9*, 864286.
14. Yeye, E.O.; Khan, K.M.; Chigurupati, S.; Wadood, A.; Rehman, A.U.; Perveen, S.; Maharajan, M.K.; Shamim, S.; Hameed, S.; Aboaba, S.A.; et al. Syntheses, in vitro α-amylase and α-glucosidase dual inhibitory activities of 4-amino-1,2,4-triazole derivatives their molecular docking and kinetic studies. *Bioorganic Med. Chem.* **2020**, *28*, 115467.
15. Sharma, P.; Thakur, A.; Goyal, A.; Grewal, A.S. Molecular docking, 2D-QSAR and ADMET studies of 4-sulfonyl-2-pyridone heterocycle as a potential glucokinase activator. *Results Chem.* **2023**, *6*, 101105.
16. Mitra, S.; Chatterjee, S.; Bose, S.; Panda, P.; Basak, S.; Ghosh, N.; Mandal, S.C.; Singhmura, S.; Halder, A.K. Finding structural requirements of structurally diverse α-glucosidase and α-amylase inhibitors through validated and predictive 2D-QSAR and 3D-QSAR analyses. *J. Mol. Graph. Model.* **2024**, *126*, 108640.
17. ChemOffice. PerkinElmer Informatics. 2016. Available online: **http://www.cambridgesoft.com** (accessed on 10 December 2023).
18. PaDEL-Descriptor Yap. An open source software to calculate molecular descriptors and fingerprints. *J. Comput. Chem.* **2011**, *32*, 1466–1474.
19. Gramatica, P.; Chirico, N.; Papa, E.; Cassani, S.; Kovarich, S. QSARINS: A new software for the development, analysis, and validation of QSAR MLR models. *J. Comput. Chem.* **2013**, *34*, 2121–2132.
20. Mauri, A.; Consonni, V.; Todeschini, R. Molecular descriptors. In *Handbook of Computational Chemistry*; Springer: Cham, Switzerland, 2017; pp. 2065–2093.
21. Gramatica, P.; Cassani, S.; Roy, P.P.; Kovarich, S.; Yap, C.W.; Papa, E. QSAR Modeling is not "Push a Button and Find a Correlation": A Case Study of Toxicity of (Benzo-)triazoles on Algae. *Mol. Inform.* **2012**, *31*, 817–835.
22. Nour, H.; Abchir, O.; Belaidi, S.; Qais, F.A.; Chtita, S.; Belaaouad, S. 2D-QSAR and molecular docking studies of carbamate derivatives to discover novel potent anti-butyrylcholinesterase agents for Alzheimer's disease treatment. *Bull. Korean Chem. Soc.* **2021**, *43*, 277–292.
23. Nour, H.; Abchir, O.; Belaidi, S.; Chtita, S. Research of new acetylcholinesterase inhibitors based on QSAR and molecular docking studies of benzene-based carbamate derivatives. *Struct. Chem.* **2022**, *33*, 1935–1946.
24. Chirico, N.; Gramatica, P. Real External Predictivity of QSAR Models. Part 2. New Intercomparable Thresholds for Different Validation Criteria and the Need for Scatter Plot Inspection. *J. Chem. Inf. Model.* **2012**, *52*, 2044–2058.
25. Bennani, F.E.; Doudach, L.; Karrouchi, K.; El Rhayam, Y.; Rudd, C.E.; Ansar, M.; Faouzi, M.E.A. 2D-QSAR study and design of novel pyrazole derivatives as an anticancer lead compound against A-549, MCF-7, HeLa, HepG-2, PaCa-2, DLD-1. *Comput. Toxicol.* **2023**, *26*, 100265.

26. Sun, G.; Zhang, Y.; Pei, L.; Lou, Y.; Mu, Y.; Yun, J.; Li, F.; Wang, Y.; Hao, Z.; Xi, S.; et al. Chemometric QSAR modeling of acute oral toxicity of Polycyclic Aromatic Hydrocarbons (PAHs) to rat using simple 2D descriptors and interspecies toxicity modeling with mouse. *Ecotoxicol. Environ. Saf.* **2021**, *222*, 112525.
27. Gramatica, P.; Sangion, A. A Historical Excursus on the Statistical Validation Parameters for QSAR Models: A Clarification Concerning Metrics and Terminology. *J. Chem. Inf. Model.* **2016**, *56*, 1127–1131
28. Nath, A.; Ojha, P.K.; Roy, K. Computational modeling of aquatic toxicity of polychlorinated naphthalenes (PCNs) employing 2D-QSAR and chemical read-across. *Aquat. Toxicol.* **2023**, *257*, 106429.
29. Gramatica, P. Principles of QSAR models validation: Internal and external. *QSAR Comb. Sci.* **2007**, *26*, 694–701.
30. Khedraoui, M.; Nour, H.; Yamari, I.; Abchir, O.; Errougui, A.; Chtita, S. Design of a new potent Alzheimer's disease inhibitor based on QSAR, molecular docking and molecular dynamics investigations. *Chem. Phys. Impact* **2023**, *7*, 100361.
31. Eriksson, L.; Jaworska, J.; Worth, A.P.; Cronin, M.T.; McDowell, R.M.; Gramatica, P. Methods for reliability and uncertainty assessment and for applicability evaluations of classification-and regression-based QSARs. *Environ. Health Perspect.* **2003**, *111*, 1361–1375.
32. Netzeva, T.I.; Worth, A.P.; Aldenberg, T.; Benigni, R.; Cronin, M.T.; Gramatica, P.; Jaworska, J.S.; Kahn, S.; Klopman, G.; Marchant, C.A. Current status of methods for defining the applicability domain of (quantitative) structure-activity relationships: The report and recommendations of ECVAM workshop 52. *Altern. Lab. Anim.* **2005**, *33*, 155–173.
33. Yamari, I.; Abchir, O.; Siddique, F.; Zaki, H.; Errougui, A.; Talbi, M.; Bouachrine, M.; ElKouali, M.; Chtita, S. The anticoagulant potential of Lippia Alba extract in inhibiting SARS-CoV-2 Mpro: Density functional calculation, molecular docking analysis, and molecular dynamics simulations. *Sci. Afr.* **2024**, *23*, e01986.
34. Ševčík, J.; Hostinová, E.; Solovicová, A.; Gašperík, J.; Dauter, Z.; Wilson, K.S. Structure of the complex of a yeast glucoamylase with acarbose reveals the presence of a raw starch binding site on the catalytic domain. *FEBS J.* **2006**, *273*, 2161–2171.
35. Guex, N.; Peitsch, M.C. SWISS-MODEL and the Swiss-Pdb Viewer: An environment for comparative protein modeling. *Electrophoresis* **1997**, *18*, 2714–2723.
36. Trott, O.; Olson, A. Software news and update AutoDock Vina: Improving the speed and accuracy of docking with a new scoring function, efficient optimization, and multithreading. *J. Comput. Chem.* **2009**, *31*, 455–461.
37. Diniyah, N.; Alam, B.; Javed, A.; Alshammari, F.H.; Choi, H.-J.; Lee, S.-H. In silico and docking studies on the binding activities of Keap1 of antioxidant compounds in non-oilseed legumes. *Arab. J. Chem.* **2023**, *16*, 104414.
38. Elangovan, N.; Sowrirajan, S.; Arumugam, N.; Almansour, A.I.; Mahalingam, S.M.; Kanchana, S. Synthesis, solvent role (water and DMSO), antimicrobial activity, reactivity analysis, inter and intramolecular charge transfer, topology, and molecular docking studies on adenine derivative. *J. Mol. Liq.* **2023**, *391*, 123250.
39. Hanwell, M.D.; Curtis, D.E.; Lonie, D.C.; Vandermeersch, T.; Zurek, E.; Hutchison, G.R. Avogadro: An advanced semantic chemical editor, visualization, and analysis platform. *J. Cheminform.* **2012**, *4*, 17.
40. Liu, X.; Zang, X.; Yin, X.; Yang, W.; Huang, J.; Huang, J.; Yu, C.; Ke, C.; Hong, Y. Semi-synthesis of C28-modified triterpene acid derivatives from maslinic acid or corosolic acid as potential α-glucosidase inhibitors. *Bioorganic Chem.* **2020**, *97*, 103694.
41. Morris, G.M.; Huey, R.; Lindstrom, W.; Sanner, M.F.; Belew, R.K.; Goodsell, D.S.; Olson, A.J. AutoDock4 and AutoDockTools4: Automated docking with selective receptor flexibility. *J. Comput. Chem.* **2009**, *30*, 2785–2791.
42. Yusuf, T.L.; Waziri, I.; Olofinsan, K.A.; Akintemi, E.O.; Hosten, E.C.; Muller, A.J. Evaluating the in vitro antidiabetic, antibacterial and antioxidant properties of copper(II) Schiff base complexes: An experimental and computational studies. *J. Mol. Liq.* **2023**, *389*, 122845.
43. Shukla, R.; Munjal, N.S.; Singh, T.R. Identification of novel small molecules against GSK3β for Alzheimer's disease using chemoinformatics approach. *J. Mol. Graph. Model.* **2019**, *91*, 91–104.
44. Yamari, I.; Abchir, O.; Nour, H.; El Kouali, M.; Chtita, S. Identification of new dihydrophenanthrene derivatives as promising anti-SARS-CoV-2 drugs through in silico investigations. *Main Group Chem.* **2023**, *22*, 469–484.

45. Duchowicz, P.R.; Talevi, A.; Bellera, C.; Bruno-Blanch, L.E.; Castro, E.A. Application of descriptors based on Lipinski's rules in the QSPR study of aqueous solubilities. *Bioorganic Med. Chem.* **2007**, *15*, 3711–3719.
46. Chagas, C.M.; Moss, S.; Alisaraie, L. Drug metabolites and their effects on the development of adverse reactions: Revisiting Lipinski's Rule of Five. *Int. J. Pharm.* **2018**, *549*, 133–149.
47. Lambring, C.B.; Fiadjoe, H.; Behera, S.K.; Basha, R. Docking and molecular dynamic simulations of Mithramycin-A and Tolfenamic acid against Sp1 and survivin. *Process. Biochem.* **2024**, *137*, 207–216.
48. Basnet, S.; Ghimire, M.P.; Lamichhane, T.R.; Adhikari, R.; Adhikari, A. Identification of potential human pancreatic α-amylase inhibitors from natural products by molecular docking, MM/GBSA calculations, MD simulations, and ADMET analysis. *PLoS ONE* **2023**, *18*, e0275765.
49. Roos, K.; Wu, C.; Damm, W.; Reboul, M.; Stevenson, J.M.; Lu, C.; Dahlgren, M.K.; Mondal, S.; Chen, W.; Wang, L.; et al. OPLS3e: Extending Force Field Coverage for Drug-Like Small Molecules. *J. Chem. Theory Comput.* **2019**, *15*, 1863–1874.
50. Protein Preparation Wizard. Available online: **https://www.schrodinger.com/science-articles/protein-preparation-wizard** (accessed on 10 March 2023).
51. Mark, P.; Nilsson, L. Structure and Dynamics of the TIP3P, SPC, and SPC/E Water Models at 298 K. *J. Phys. Chem. A* **2001**, *105*, 9954–9960.
52. Uba, A.I.; Chea, J.; Hoag, H.; Hryb, M.; Bui-Linh, C.; Wu, C. Binding of a positive allosteric modulator CDPPB to metabotropic glutamate receptor type 5 (mGluR5) probed by all-atom molecular dynamics simulations. *Life Sci.* **2022**, *309*, 121014.
53. D.E. Shaw Research. *Desmond Molecular Dynamics System, Maestro-Desmond Interoperability Tools*; Schrödinger: New York, NY, USA, 2021.
54. Bhattacharya, P.; Abualnaja, K.M.; Javed, S. Theoretical studies, spectroscopic investigation, molecular docking, molecular dynamics and MMGBSA calculations with 2-hydrazinoquinoline. *J. Mol. Struct.* **2023**, *1274*, 134482.
55. Adeniji, S.E.; Uba, S.; Uzairu, A. Theoretical modeling and molecular docking simulation for investigating and evaluating some active compounds as potent anti-tubercular agents against MTB CYP121 receptor. *Futur. J. Pharm. Sci.* **2018**, *4*, 284–295.
56. Huang, X.; Ma, S.; Wu, Y.; Wan, C.; Zhao, C.; Wang, H.; Ju, S. High-Throughput Screening of Amorphous Polymers with High Intrinsic Thermal Conductivity via Automated Physical Feature Engineering. *J. Mater. Chem. A* **2023**, *11*, 20539–20548.
57. Mouhsin, M.; Abchir, O.; El Otmani, F.S.; Oumghar, A.A.; Oubenali, M.; Chtita, S.; Mbarki, M.; Gamouh, A. Identification of novel NLRP3 inhibitors: A comprehensive approach using 2D-QSAR, molecular docking, molecular dynamics simulation and drug-likeness evaluation. *Chem. Pap.* **2023**, *78*, 1193–1204.
58. Yang, L.; Wang, Y.; Hao, W.; Chang, J.; Pan, Y.; Li, J.; Wang, H. Modeling pesticides toxicity to Sheepshead minnow using QSAR. *Ecotoxicol. Environ. Saf.* **2020**, *193*, 110352.
59. Papa, E.; Sangion, A.; Arnot, J.A.; Gramatica, P. Development of human biotransformation QSARs and application for PBT assessment refinement. *Food Chem. Toxicol.* **2018**, *112*, 535–543.